

Simulations of buoyant flows driven by variations in solar radiation beneath ice cover

Donovan J. M. Allum¹* and Marek Stastna¹*Department of Applied Mathematics, University of Waterloo, Waterloo, Ontario, Canada N2L 3G1*

(Received 23 December 2023; accepted 8 May 2024; published 17 June 2024)

Spatial variations in ice and snow characteristics imply that radiative forcing in late winter lakes is spatially heterogeneous. We present idealized, three-dimensional simulations of buoyancy-driven flows, driven in this setting with heterogeneous solar radiation intensity, comparing rectilinear and radial cases. In both cases, radiative forcing in fresh water at temperatures below 4 °C initiates an unstable stratification near the surface, leading to Rayleigh-Taylor instabilities. The variations in radiative forcing intensity generates gravity current-like flow along the surface. The resulting flow interacts with developing three-dimensional Rayleigh-Taylor instabilities. We provide an in-depth analysis of the development and death of the gravity current-like flow in the two cases mentioned. We find that while the interaction of this current with radiatively driven convection does create instabilities along the leading edge and slow its propagation, it is mixing with the convective and warm return flow that leads to the cessation of propagation and eventual death of the current. Differences in geometry affect the depth of the shear layer between the current and return flow, determining the timing of when propagation ends.

DOI: [10.1103/PhysRevFluids.9.063501](https://doi.org/10.1103/PhysRevFluids.9.063501)

I. INTRODUCTION

Most lakes have ice cover during the winter season [1–5]. The ice cover in these lakes is occasionally multiyear ice [2,3] but is most often single-year ice cover. This means that at some point during the year the lake freezes over and at a later point near the end of the winter the ice-cover breaks, leading to ice-free conditions [1,3,5–7]. These dates are known as the freezing and break-up dates, respectively. In these lakes, due to Climate Change, freezing dates occur later and break-up dates occur earlier than in the past, and this trend is expected to continue [1,4–6,8]. Neither the break-up date nor the freezing dates are typically defined such that they require 0% or 100% ice coverage, and as a result, spatial variability in ice coverage is common between the freezing and break-up date [7,9–12]. In order to develop a more complete understanding of the distribution of heat and convection under ice, spatial variability in optical properties in the ice or snow cover must be considered.

Late in the winter after the snow layer on top of the ice melts, solar radiation becomes a key driver of motion under ice [3,13–16]. Snow has a higher albedo than ice [3,10,17], and, as a result, significant solar radiation is able to penetrate the ice into the water column after the snow melts [15,17–19]. Temperatures under ice-covered lakes are below the temperature of maximum density ($T_{MD} \approx 4$ °C), hence, solar radiation gradually destabilizes the water column, driving convection in the vertical and the development of a convective mixed layer [13,15,18,20]. Convection driven by solar radiation is called radiatively driven convection (RDC) or penetrative convection (PC) in lakes with a stable background stratification. Studies on RDC or PC under ice typically assume that the

*dallum@uwaterloo.ca

optical properties of ice are uniform [15,18,21]. Studies that analyze the effect of spatial variability in optical properties on convection and buoyancy driven flows are rare.

To the authors' knowledge, at the time of writing, only one such study exists [22]. Reference [22] is a process study that uses two-dimensional numerical simulations to show that sharp changes in solar radiation intensity generate intrusions along the surface that flow from the region where solar radiation is damped towards the region where RDC is ongoing. This study further examined the variation of key parameters such as the percentage change in sunlight intensity, the initial temperature of the system, and the light attenuation. Each parameter has a unique effect on the intrusion and the development of RDC.

The intrusion discussed in Ref. [22] is a special case of a buoyancy-driven flow called a gravity current. A gravity current is a type of flow where mass is transported in a direction perpendicular to gravity [23] due to a difference in density in the same direction, either within a single fluid or between different fluids, such as the classic example of oil and water. Gravity currents generated by a lock exchange are initially two-dimensional with negligible variation in the transverse. However, as the current develops, features along the head, at the contact boundary (in the case of no-slip boundary conditions), and at the interface between the intruding and ambient fluid develop much differently in two dimensions compared to three [23–27].

The simplest example of a gravity current is one generated by a lock exchange. A physical boundary is set at the start of an experiment—numerical or laboratory—where the physical boundary divides the ambient and intruding fluid. The boundary is removed at the onset of the experiment [23]. Sometimes the ambient and intruding fluids are different fluids entirely, but often they are the same fluid at different densities. In the lock-exchange literature, two configurations are most commonly studied: (1) the planar or two-dimensional gravity current, and (2) the axisymmetric or cylindrical gravity current [26–31]. These are convenient configurations primarily because they both can be simulated and analyzed analytically as if they are in two dimensions, a planar current in the xz plane in Cartesian coordinates, and an axisymmetric current in the rz plane in polar coordinates. It is then implicitly assumed that the current does not vary in the transverse: y for planar currents and the azimuthal direction (often denoted as θ) for axisymmetric currents. Reference [28] is an especially important paper that provides analytical solutions for the evolution of a planar and axisymmetric gravity current during the slumping phase (see more about these phases in Chapter 12 of Ref. [23] and [31]). Further analytical progression in three dimensions is likely not possible; however, the equations derived in Ref. [28] have been compared with experiments with good agreement [26,28].

Gravity current studies that include axisymmetric three-dimensional simulations, while less common compared to the rectangular case, are available in the literature [26,27,31]. Reference [31] compares two- and three-dimensional simulations of both planar and cylindrical/axisymmetric gravity currents. The two-dimensional axisymmetric current is simulated by solving the two-dimensional Navier-Stokes equations in cylindrical coordinates. Both high Reynolds number ($Re = 8950$) and low Reynolds number ($Re = 895$) values were considered. The three-dimensional cylindrical and planar currents remained largely two-dimensional for the lower Re cases for the full duration of their evolution. It is reasonable to expect that three-dimensional extensions of the simulations in Ref. [22] are at least initially two-dimensional but should become three-dimensional as the intrusion interacts with the convective ambient and features at the boundary of the intrusion and the ambient breakdown. Reference [26] looked at cylindrical gravity currents subjected to rotation, finding significant azimuthal symmetry at all times in a comparative nonrotating case and up to one-tenth of a revolution for slowly rotating cases. Reference [27] generates an axisymmetric gravity current by placing a small opening in a large wall separating two fluids of different densities. Fluid is exchanged symmetrically and then propagates outward radially from the opening, along the surface for the lighter fluid and along the bottom for the heavier fluid. To date, there only exist two papers that document simulations of three-dimensional gravity currents in the cold-water regime [32,33], although there have been several papers in two dimensions [18,22,34,35]. Reference [33] is from a theoretical lens, and Ref. [32] is of a more geophysical lens with some theoretical analysis, similar to Ref. [18].

In this paper, we present three-dimensional simulations of intrusions generated by sharp changes in solar radiation intensity. These simulations are three-dimensional extensions of Ref. [22]. However, due to the enhanced computational costs, a sweep of the parameter space is not possible. Instead, we consider one simulation that has a rectangular region where the solar radiation is “damped” or shadowed at the edge of the domain and another where the shadowed region is circular at the corner of the domain. As in Ref. [22], intrusions are generated along the shadow boundary away from the shadowed region, into the region with freely developing RDC. The goal of this paper is to compare and contrast the geometry of the shadow and its effect on the intrusion, an analysis that is not possible in two dimensions.

II. METHODS

A. Equations of motion and numerical model

We use the nonhydrostatic, pseudospectral model SPINS [36] to solve the incompressible Navier-Stokes equations under the Boussinesq approximation to produce the direct numerical simulations presented in this paper:

$$\frac{D\vec{u}}{Dt} = -\frac{1}{\rho_0}\vec{\nabla}p + \nu\nabla^2\vec{u} - g\frac{\rho}{\rho_0}\hat{k}, \quad (1a)$$

$$\vec{\nabla} \cdot \vec{u} = 0, \quad (1b)$$

$$\frac{DT}{Dt} = \kappa_T\nabla^2T + \frac{Q_0}{\lambda}\exp\left(-\frac{(L_z - z)}{\lambda}\right)F(x, y). \quad (1c)$$

Equation (1a) is the momentum equation to determine the fluid velocity, \vec{u} . Equation (1b) is the incompressibility condition. Equation (1c) is the temperature, T , evolution equation. p is the pressure and ρ is the density perturbation from the background, ρ_0 . SPINS has been previously applied to a wide variety of scenarios to produce accurate, high-resolution simulations in the cold-water regime as well as other dynamical regimes [22,33–35,37]. The last term in the temperature equation is the radiative forcing term that obeys the single-band, Beer-Lambert law [3]. The single-band Beer-Lambert law has been used in similar simulations of RDC [18,21,22,32]. The horizontal structure, $F(x, y)$, is given below in Sec. II B.

The density, ρ , is determined from the temperature via an approximation to the UNESCO equation of state [38], shifted so that the maximum temperature coincides with 4°C. This shifted equation of state has been previously applied to simulations of cold-water convection [22,34]. The vorticity equation is also relevant to this analysis,

$$\frac{D\vec{\omega}}{Dt} = (\vec{\omega} \cdot \nabla)\vec{u} + \frac{g}{\rho_0}\left(-\frac{\partial\rho}{\partial y}, \frac{\partial\rho}{\partial x}, 0\right) + \nu\nabla^2\vec{\omega}, \quad (2)$$

where this is obtained in the usual manner of taking the curl of the momentum equation (1a). The second term, the baroclinic term, is especially relevant to the analysis of this paper as it directly captures how horizontal density differences initialize rotation. The enstrophy, computed as $0.5|\vec{\omega}|^2$, is also used to discuss the degree of mixing in the interior of the intrusion.

B. System of interest

In Ref. [22] the shadow was placed in the center of the domain with unshadowed regions on either side. This resulted in two intrusions that traveled in opposite directions along the surface away from the shadowed region. In order to maximize spatial resolution, as well as the physical extent of the domain for the development of RDC, in this paper the shadowed regions are placed at the edge of the domain, and only a single intrusion will be produced along the surface.

There are three cases that we will consider in this paper, listed in Table I, each of which has identical physical parameters to those used in Ref. [22]. The physical and system parameters are

TABLE I. Table of cases. For the full list of parameters see Table II. When referring to one of these cases in the text the case name in this table will be used. The difference between the two cases with a quarter circle is that the No Noise case has no noise seeded in its initial conditions.

Case name	Shadow shape
Corner	Quarter circle
Slat	Rectangular
No Noise	Quarter circle

given in Table II. The velocity boundary conditions are free-slip everywhere, and the temperature boundary conditions are no-flux. The initial conditions are constant temperature, T_0 . The first case, called the Corner case, is a system subjected to solar radiation with a circular shadowed region at the corner of the rectangular domain. The intrusion propagates in the radial, r , outward direction with symmetry in the azimuthal, θ , direction. The intrusion generated using this geometry is often called an axisymmetric or cylindrical gravity current [26,28,30]. The second case, called the Slat case, is where the shadow is rectangular and extends the entirety of the y domain. This is typically referred to as two-dimensional spreading [28], or a current along a channel [30]. In the Slat case, the symmetry is in the y dimension, rather than in the azimuthal direction as in the Corner case. As a result, the intrusion will propagate in the x direction and less horizontal extent (y direction) is required. A schematic for the side view and a to scale, top-down view for both cases is given in Fig. 1. The final case is the No Noise case. Due to the high-order nature of the numerical method used in SPINS [36], some kind of perturbation is required in the initial conditions for the development of instabilities that grow from small perturbations in the flow. Noise is seeded in the velocity fields of the Corner and Slat cases with a normal distribution of mean zero and standard deviation of $3 \times 10^{-3} \text{ ms}^{-1}$.

All three cases share the same length scales except for the smaller L_y in the Slat case and the difference in geometry. L_y was shortened in the Slat case to reduce the computational cost but not so

TABLE II. Parameters used in this paper. The upper table gives the physical parameters that do not change between configurations (see Fig. 1). The lower table gives the domain size and resolution parameters. A dash indicates that the parameter is the same as in the Corner case.

Parameter	Description	Value		
T_0	Initial temperature	$2.5 \text{ }^\circ\text{C}$		
λ	Attenuation coefficient	0.4 m		
ρ_0	Reference density	1000 kg m^{-3}		
ν	Kinematic viscosity	$10^{-6} \text{ m}^2 \text{ s}^{-1}$		
κ	Temperature diffusivity	$1.43 \times 10^{-7} \text{ m}^2 \text{ s}^{-1}$		
Q_0	Kinematic radiative flux	$7.17 \times 10^{-5} \text{ }^\circ\text{C m s}^{-1}$		
A_l	Albedo	0.9		
w_d	Shadow width	2 m		
Parameter	Description	Corner	No Noise	Slat
L_x	Lake width	10.24 m	–	–
L_y	Lake length	10.24 m	–	2.56 m
L_z	Lake depth	2.56 m	–	–
N_x	X grid points	2048	–	–
N_y	Y grid points	2048	–	512
N_z	Vertical rid Points	512	–	–

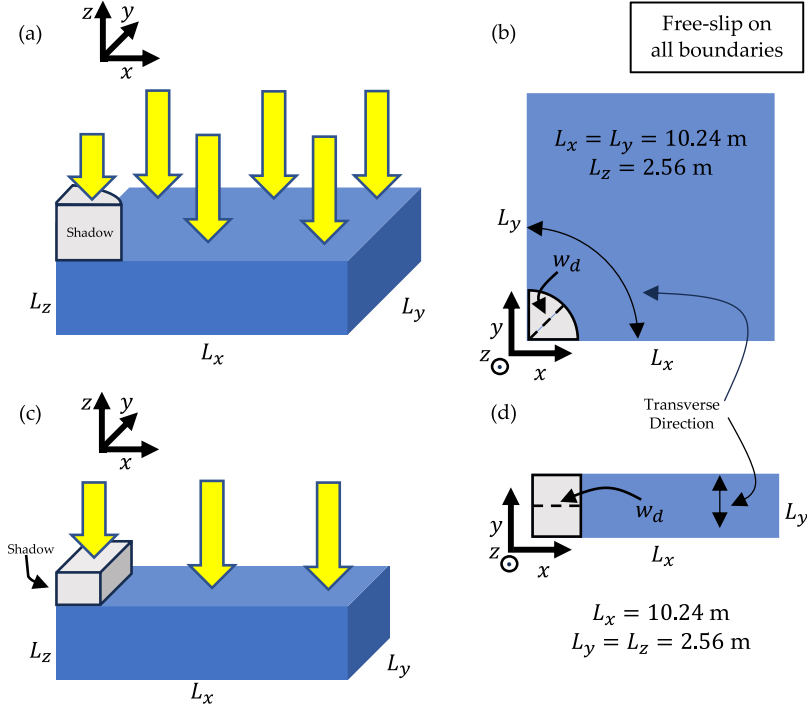


FIG. 1. Schematic depicting the two main systems. The first row (a), (b) shows the schematic for the circular shadow, and the second row (c), (d) illustrates the schematic for the rectangular shadow. In the first column (a), (c), a three-dimensional view of each configuration is presented. The shadowed region is depicted by the gray shape, and the incoming solar radiation is represented by the yellow arrows. The second column (b), (d), gives a top-down view of both systems where the shadow and domain size are to scale. Parameter values are listed in Table II.

much as to modify how the convective cells develop at late times ahead of the intrusion. Sufficient space was required to allow the intrusion to develop without interacting with the far walls. The important parameter in this case is w_d/L_x , where w_d is the width or radius of the shadowed region (see Fig. 1 and Table II). The simulations here use a value of $1/4$. Simulations with a value of $1/2$ were attempted but found to be insufficient. The depth, L_z , chosen is comparable to many small lakes with ice cover during the winter in Canada's north [9,39,40]. Large ice floes comparable in size to the shadowed region have been observed on ice-covered lakes [11]. The simulations presented in this paper are meant to be a simplified system to analyze geometrical effects on this radiatively driven intrusion, a three-dimensional extension of [22].

$F(x, y)$ in the forcing term of the temperature equation (1c) is a smooth function that determines the horizontal changes to the intensity of the solar radiation. The other parameters are defined in Table II. For the Slat case,

$$F(x, y) = \left[1 - A_l \exp\left(-\frac{x^{8w_d}}{w_d^{8w_d}}\right) \right], \quad (3)$$

where A_l is the albedo quantifying the loss in radiative forcing under the shadowed region and w_d is the width of the shadowed region, depicted in Fig. 1. Equation (3) is similar to the form used in Ref. [22] but with the shadow at the edge of the domain instead of at its center. In the Corner case,

$$F(x, y) = \left[1 - A_l \exp\left(-\frac{(x^2 + y^2)^{4w_d}}{w_d^{8w_d}}\right) \right],$$

where the coefficient in the exponent is reduced from 8 to 4 due to a cancellation of a square root. The intrusions generated in the Slat and Corner cases are distinct from classical gravity currents due to the time-varying nature and the unstable stratification away from the shadowed region. For the remainder of this paper, the y direction in the Slat case and the θ direction in the Corner case will be discussed concurrently and will be referred to as the transverse direction in both cases for simplicity, as it is labeled on Figs. 1(b) and 1(d).

C. Averaging notation

In this paper, several forms of averaging (Horizontal, vertical, azimuthal, and domain averaging) will be used to present the results. For averages computed in the horizontal in Cartesian coordinates we will use the notation

$$\langle f \rangle_i = \frac{1}{L_i} \int_0^{L_i} f dx_i, \quad (4)$$

where f is an arbitrary scalar function, and i refers to the direction that the average is computed. Multiple indices indicate that the average was computed over each dimension.

In the Corner case, the intrusion propagates in the outward radial direction; hence, averages computed using cylindrical coordinates will be useful. Consider a cylindrical region of arbitrary height and radius R . Set the origin at the center of this region with the z axis aligned with the cylinder. An azimuthal average over this cylinder at height z is computed by taking the integral over a cylindrical shell of thickness Δr at radius r . The average is computed as

$$\langle f \rangle_\theta = \frac{\int_0^{\pi/2} \int_r^{r+\Delta r} f[r \cos(\theta), r \sin(\theta), z] r d\theta}{\int_0^{\pi/2} \int_r^{r+\Delta r} r dr d\theta}. \quad (5)$$

This azimuthal average is computed numerically by defining a shell thickness, Δr , and summing the scalar quantity inside the shell at each z and dividing by the approximate area in the region. This type of averaging scheme is only necessary because SPINS is discretized in Cartesian coordinates. A simulation discretized in cylindrical coordinates could perform this averaging more simply.

Another quantity related to the average which will be used in the analysis presented in this paper is the variance along the direction of propagation. We write the variance of the variable, f , as $\sigma^2(f)$. The variance is computed for the Corner case as

$$\sigma^2(f) = \langle \langle f^2 \rangle_\theta \rangle_z - \langle \langle f \rangle_\theta \rangle_z^2, \quad (6)$$

and for the Slat case as

$$\sigma^2(f) = \langle \langle f^2 \rangle_y \rangle_z - \langle \langle f \rangle_y \rangle_z^2. \quad (7)$$

In both cases, σ^2 is a function of distance along the direction of propagation, r for the Corner case and x for the Slat case.

D. Quantifying the intrusion height

A classical, lock-exchange gravity current typically has a density difference between the ambient and intruding fluid that is fixed in time [23]. Reference [31] is an example of a measure of the height of a gravity current. The height is estimated by integrating the nondimensional density over the vertical direction. The density is scaled such that the intruding fluid has a density of one and the ambient has a density of zero. By construction, a column of fluid entirely consisting of the intruding fluid will have a height of L_z and a column of fluid consisting entirely of the ambient will have a height of zero.

This definition is useful because it accounts for mixing along the interface between the gravity current and the ambient. A problem with this approach for the simulations outlined in this paper is that it does not account for the ambient gradually increasing in temperature and the interior of

the intrusion gradually warming due to the external solar radiation forcing. As a result, this measure quickly loses track of the intrusion even as fluid continues to be transported away from the shadowed region. Instead, we use the following definition for the Corner case:

$$G(z, t) = \frac{1}{L_C(t) - w_d} \int_{w_d}^{L_C(t)} \langle u_r \rangle_\theta dr, \quad (8)$$

where $G(z, t)$ is simply $\langle u_r \rangle_\theta$ averaged in the r direction from the shadow boundary ($r = w_d$) to the intrusion front $r = L_C(t)$ (see Sec. II E). The height is then determined by setting

$$G(z, t) = 0$$

and solving for z . For the Slat case,

$$G(z, t) = \frac{1}{L_S(t) - w_d} \int_{w_d}^{L_S(t)} \langle u \rangle_y dx, \quad (9)$$

where $L_S(t)$ is the front position and the height of the intrusion is again determined by setting $G(z, t)$ to zero.

E. Intrusion front position

For both the Corner and Slat case, the front position was initially identified as the maximum of $\langle T \rangle_\theta$ (Corner) and $\langle T \rangle_y$ (Slat) at $z = L_z$, the temperature field averaged in the transverse direction. The maximum temperature for these fields is located at the front position and extends down the parabolic leading edge. The boundary between the intrusion and the convective ambient is so thin that the temperature at the front is entrained by the intrusion and not well mixed, as well as continuously heated by solar radiation. Fluid farther ahead of the intrusion is more easily mixed and slightly cooler and fluid behind the front is always cooler.

After enough time had elapsed, the intrusion front position is no longer possible to identify using $\langle T \rangle_\theta$ or $\langle T \rangle_y$. This can be seen in Fig. 4 or 5, in the left column of each figure. At later times, we instead use the same averages but applied to the velocity of the fluid parallel to the intrusion propagation direction. For the Corner case, this is the radial velocity, u_r , and for the Slat case this is the x velocity, u . Unlike $\langle T \rangle_\theta$ or $\langle T \rangle_y$ the maximum value of $\langle u_r \rangle_\theta$ or $\langle u \rangle_y$ is not located near the intrusion front, to be discussed in Sec. III A. Instead, the front position was identified as the edge of the region in $\langle u_r \rangle_\theta$ and $\langle u \rangle_y$ near the surface that is modified by the intrusion. In Sec. III A, it is shown that this edge is qualitatively clear but still difficult to define rigorously. For these later times, the front position was chosen as the position that best aligned visually with the intrusion front in u_r and u , with both the average but also in conjunction with horizontal slices in the velocity field.

1. Froude number

The Froude number is considered an important dimensionless parameter in the analysis of gravity currents. In the case of a classical gravity current with an intruding and ambient fluid, each with uniform density, the Froude number is written as

$$\text{Fr} = \frac{U}{\sqrt{g' L_z}}, \quad (10)$$

where U is the front velocity of the gravity current and $\sqrt{g' L_z}$ is a velocity scale set by the reduced gravity, $g' = (\rho_1 - \rho_2)/\rho_0$, and the height of the current in the initial conditions. In deep water at high Reynolds number, Uh/ν , the Froude number is thought to be equal to $2^{1/2}$ [23,30,41]. The Froude number has also been shown to depend on the fractional depth, h/L_z , of the gravity current compared with the domain height for shallow domains [28,30].

If we define g' in the system presented in this paper in terms of the density just in front and just behind the intrusion, we can see that g' is no longer constant as the density difference under and away from the shadowed region increases with time. The background temperature at early times is approximated by

$$\frac{\partial T_b}{\partial t} = \frac{Q_0}{\lambda} \exp\left(-\frac{(L_z - z)}{\lambda}\right) [A_l \theta(x - w_d) + (1 - A_l)], \quad (11)$$

where $\theta(x)$ is the Heaviside function. Assuming a linear equation of state

$$\rho(T) - \rho_0 = \alpha \rho_0 (T - T_0), \quad (12)$$

where $\alpha \approx 2.2 \times 10^{-5} \text{ C}^{-1}$, which is reasonable for small temperature differences even below T_{MD} . A further complication is the stratification induced by Eq. (11), which means that g' is also a function of depth.

Gravity currents in a stably stratified ambient have been studied in the literature [23,42,43], where the Froude number is written in terms of the Buoyancy frequency,

$$N = \sqrt{\frac{g}{\rho_0} \frac{\partial \rho}{\partial z}}. \quad (13)$$

This is problematic for the cases presented here due to the unstable stratification induced by the radiative flux in Eq. (1c), leading to an imaginary N . Further, it can be difficult to define a single value to represent the density gradient to compute a single value for the Froude number.

III. RESULTS

In the previous work on this topic [22], a set of two-dimensional simulations were presented in order to probe the parameter space of the intrusion. As we expand our interests to three-dimensional simulations, while maintaining (1) the label of high-resolution direct numerical simulations, and (2) the large vertical and horizontal length scales, a full analysis of the parameter space is less practical. Hence, this paper consists of the analysis of the three cases: Corner, Slat. and No Noise, as listed in Table I. The initial development of the intrusion in each of these cases is presented in Fig. 2 using the temperature field (color) and velocity field (arrows). We find that all three cases produce an intrusion that propagates away from the shadow region. The advance of the intrusion in the Slat case persists for longer and is generally deeper than the Corner case. Despite this, the intrusion in both the Corner and Slat cases propagates at approximately the same constant speed after an initial acceleration phase. The front ceases progression in the Corner case due to mixing with the turbulent and warm return flow. The source of the height difference is geometrical, and unlike classical gravity currents, the height of the intrusion increases with time [26,31]. Comparatively, the No Noise case gradually speeds up throughout the experiment and never ceases outward flow. However, the depth of the intrusion gradually decreases.

A. Summary of motion

In the precursor to the research presented in this paper [22] the development of RDC was divided into two phases: (1) the solar radiation dominated phase and (2) the convection-dominated phase. The distinction of these phases is characterized by the effect of convection on the mean temperature profile away from the shadowed region and ahead of the intrusion. Reference [22] shows that initially there are only negligible deviations from the background temperature field determined by solar radiation alone during the solar radiation-dominated phase. In the convection-dominated phase, there is significant deviation from the background temperature field. The transition between these two phases starts first at the surface and gradually extends towards the bottom as Rayleigh-Taylor instabilities exchange heat with the unheated fluid below. It is possible that the timing of this transition coincides with some critical Rayleigh (Ra) or Grashof (Gr) number, as in

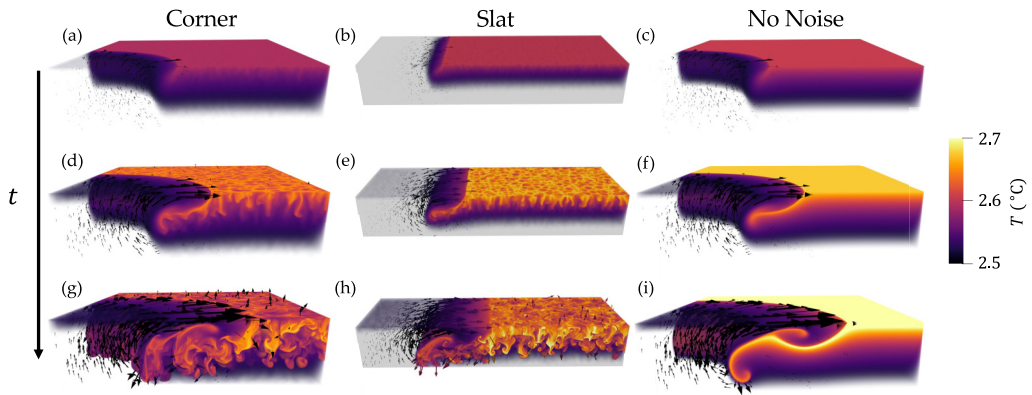


FIG. 2. Initial development in intrusions for the (a), (d), (h) Corner case, (b), (e), (i) Slat case, and (c), (f), (j) No Noise case at (a), (b), (c) $t = 600$ s, (d), (e), (f) $t = 1000$ s, and (g), (h), (i) $t = 1400$ s. Color denotes the temperature field, and the arrows denote the velocity field. There are 3000 arrows, randomly distributed, with sizes proportional to the velocity field and comparable between panels. All cases show only the top half of the domain. The Corner and No Noises cases have been truncated by 25% in both x and y . The Slat case is truncated in only x by 25%.

Rayleigh-Bénard convection. Gr in the cold-water regime for a linear equation of state [22,34] (valid for $O(0.01-0.1\text{ }^\circ\text{C})$ temperature variations, far from T_{MD}) and a nonlinear equation of state [21,33] have been reported. There are many other studies which examine Rayleigh-Bénard convection near the temperature of maximum density [44-46]. To the authors' knowledge, an examination of a time-varying stratification and the transition to convection does not exist but is not the focus of the present paper and could be the subject of future work.

In two dimensions, with the same parameters as this paper, the transition was observed at $t \approx 1000$ s. The transition in three dimensions was found to occur slightly later at $t \approx 1200$ s. The reason for the difference in timing of the transition is likely a combination of dynamical differences between two and three dimensions, as well as filtering. Due to the problem of aliasing and spectral blocking [47,48] that is inherent in spectral methods, a filter is required to remove energy at the smallest scales. However, in three dimensions a filter removes a larger fraction of the wave number space compared to two dimensions.

Figure 2 shows the development of an intrusion that propagates away from the shadowed region, as early as the solar radiation-dominated phase [Figs. 2(a)-2(f)] and into the convection-dominated phase [Figs. 2(g)-2(i)]. A schematic of the flow as viewed from the side is given in Fig. 3. Underneath the intrusion, a return flow develops with two parts. Immediately below the intrusion is the warm return flow that forms into a sideways Rayleigh-Taylor-like instability. In the Corner and Slat cases, there are many features along the warm return flow, whereas, in the No Noise case, the warm return flow is smooth. The return flow extends to the bottom, consisting of cool, unheated ambient fluid with no discernible features. The return flow is generated by conservation of volume as the fluid under the shadow flows away from the shadowed region. The warm return flow initially propagates towards the shadowed region, but at a later time [Figs. 2(g)-2(i)] due to the shear interface (Labeled on Fig. 3, parallel to the surface away from the shadowed region with a vertical component at the shadow boundary) the head of the warm return flow curls towards the surface, generating a large Kelvin-Helmholtz (KH) billow. KH billows are commonly observed in the tail of a gravity current with sufficiently large Reynolds number [23,31,49]. The Richardson number (Ri) determines the stability of a shear interface to the development of KH billows [50]. Ri is defined as the ratio of the buoyancy force to the magnitude of the shear term. Ri can be written—

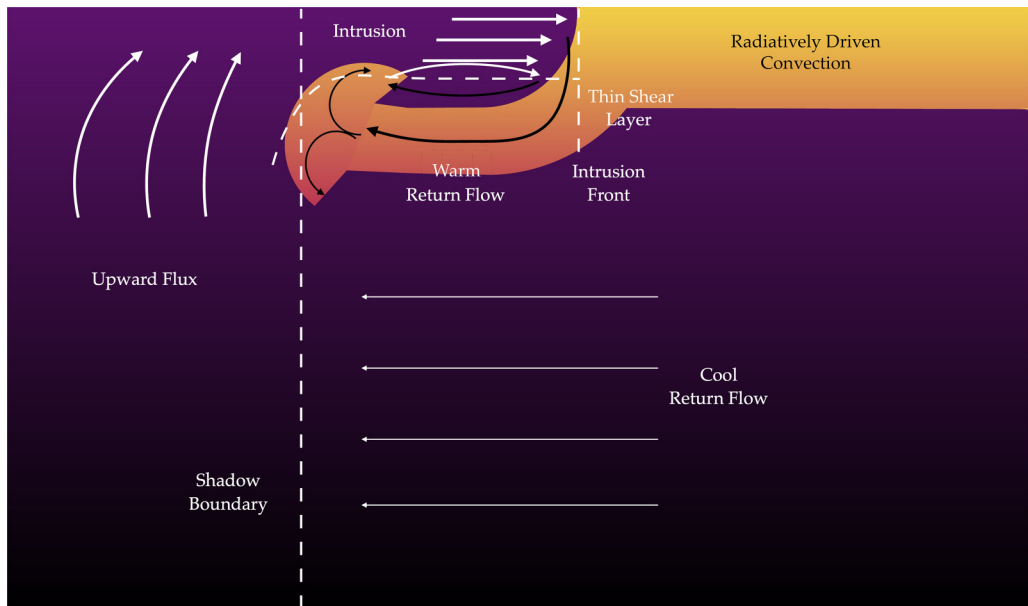


FIG. 3. Flow schematic for the dynamics presented in this paper, viewed from the side or as an average in the transverse, focused on the intrusion. This stage of motion is representative of the temperature field $t \approx 1200$ s. Arrows indicate the mean direction of motion in this plane and are colored to enhance contrast only.

under certain simplifying assumptions—as a ratio of the shear interface height to the lock height, multiplied by $1/4$.

1. Transverse averages of T and the outward velocity component

The development of the intrusion, from initial stages to collapse in the temperature field, can be seen clearly in the left column of Fig. 4 for the Corner case and Fig. 5 for the Slat case. The left column of both figures gives the temperature field averaged in the transverse direction. $\langle T \rangle_\theta$, computed using Eq. (5) for the Corner case and $\langle T \rangle_y$ using Eq. (4) for the Slat case. The right column of Figs. 4 and 5 gives the velocity in the direction parallel to the direction of propagation, $\langle u \rangle_y$ for the Slat case and $\langle u_r \rangle_\theta$ for the Corner case. These cases will be compared and contrasted side by side. In doing so, the terms “outward” and “inward” will be used in both cases to refer to motion away from and towards the wall at $x = 0$ m in the Slat case or the corner at $r = 0$ m (equivalently, $(x, y) = (0, 0)$ m).

The initial development for both cases is quite similar [Figs. 4(a) and 4(b) and Figs. 5(a) and 5(b)]. The intrusion is visible only in a small region near the shadow boundary (r or $x = 2$ m, Fig. 3). The horizontal density gradient generates vorticity along the shadow boundary, rotating the vertical temperature interface outward into the warm ambient [Figs. 4(a) and 5(a)]. This effect appears in $\langle u \rangle_{\theta/y}$ as a triangularly shaped region of outward flow towards the ambient. Flow velocity is strongest at the surface and weakest near a depth of λ where the horizontal temperature and density differences are smaller. In both cases, a region of weak flow towards the left is visible beneath the triangular region. As we will see later, this is the end of the initial growth phase where the pace of the intrusion increases (in the first 600 s of each simulation).

At the next stage, Figs. 4(c) and 4(d) and 5(c) and 5(d), the intrusion transforms into the shape of a classical gravity current typical of a free-slip surface with a parabolic shaped front edge [51] consistent with the flow schematic in Fig. 3. The intrusion at this stage is also consistent with

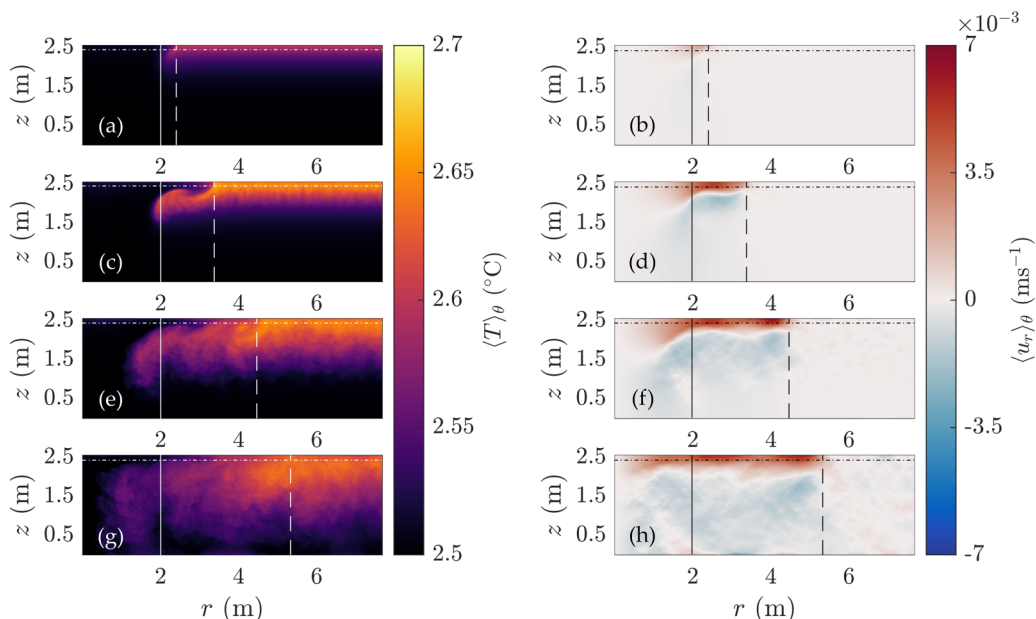


FIG. 4. T and u_r averaged in the azimuthal direction for the Corner case. Azimuthally averaged (a), (c), (e), (g) T and (b), (d), (f), (h) u_r at (a), (b) $t = 600$ s, (c), (d) $t = 1200$ s, (e), (f) $t = 1800$ s, and (g), (h) $t = 2400$ s. The vertical solid line gives the shadow boundary, set by w_d . The vertical dashed line in each panel gives the approximate front position as a function of time, given in full in Fig. 7. The horizontal dot-dashed line in each panel gives the depth of the slices in Figs. 6(a) and 6(b).

gravity currents with no-slip boundary conditions at very low Reynolds number ($Re < 1$) [30]. The warm return flow underneath begins to resemble the typical mushroom shape of a Rayleigh-Taylor instability. Both the size of the head and the thickness of the neck of the return flow are smaller in the Slat case. This is possibly due to conservation of volume as the return flow propagates inward and instead expands downwards.

In both cases, $\langle u_r \rangle_\theta$ and $\langle u_y \rangle_\theta$ exhibit a consistent outward flow along the surface, a slightly weaker inward flow in the warm return flow, and a significantly weaker flow in the cool return flow towards the bottom towards. The shear layer is mostly horizontal except at the head of the warm return flow and at the intrusion front (Fig. 3). The downwards angle of the shear layer bisects the head of the warm return flow from its neck. This is similar to the normal development of a Rayleigh-Taylor instability, where the velocity of the neck is in the direction of propagation and the velocity of the head is towards either side of the instability. At this stage of the motion, the velocity scale in the interior of the intrusion and return flow greatly exceeds the convective velocity scales ahead of the intrusion.

At the third stage, Figs. 4(e) and 4(f) and 5(e) and 5(f), the upper edge of the return flow has become a KH billow and has curled up into a vortex, which we will refer to here as the return flow vortex. Others will inevitably follow, but this vortex is crucial to the development and mixing of the intrusion in the temperature field. In both cases, the return flow vortex travels in the same direction as the intrusion as a faster rate. In the Corner case, the return flow vortex develops more rapidly and catches up to the intrusion front position at $t = 1800$ s [Figs. 5(e) and 5(f)]. In the study of classical gravity currents, especially those bounded by a wall in the direction behind the current, an effect where the return flow catches up to the front of the current has been observed and well documented [23]. However, the return flow vortex is clearly generated by a KH instability along the shear layer between the warm return flow and the intrusion, and not an interaction with the return flow and a wall behind the intrusion.

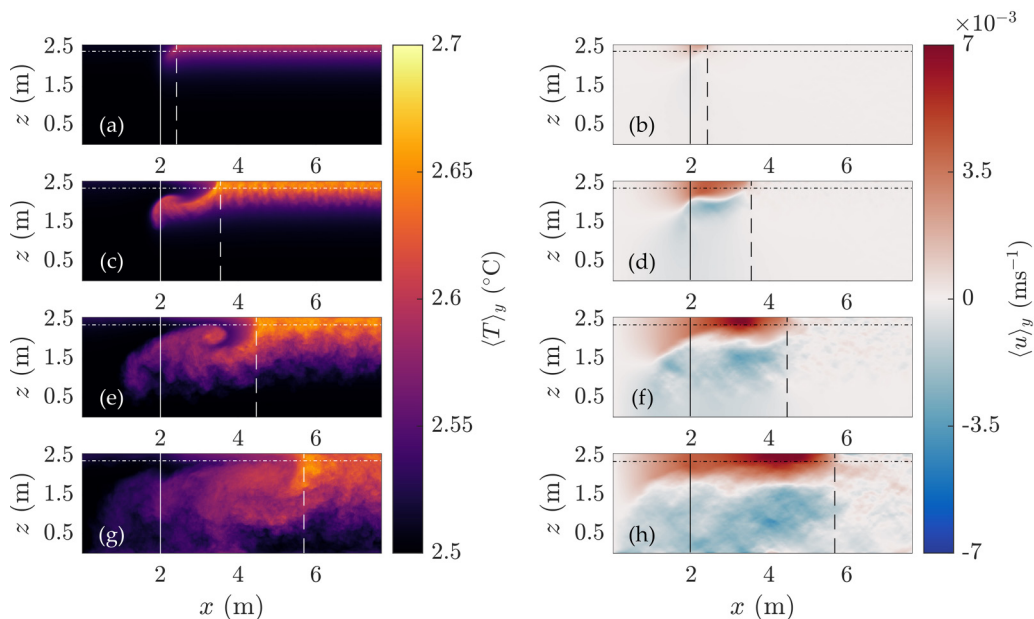


FIG. 5. T and u averaged in the y direction for the Slat case. y averaged (a), (c), (e), (g) T and (b), (d), (f), (h) u at (a), (b) $t = 600$ s, (c), (d) $t = 1200$ s, (e), (f) $t = 1800$ s, and (g), (h) $t = 2400$ s. The vertical solid line gives the shadow boundary, set by w_d . The vertical dashed line in each panel gives the approximate front position as a function of time, given in full in Fig. 7. The horizontal dot-dashed line in each panel gives the depth of the slices in Figs. 6(c) and 6(d).

There is a notable difference between the Slat and Corner cases regarding the development of the return flow vortex. In the Corner case, the collapse of the intrusion in the temperature field is evident compared to the Slat case, as shown in Figs. 4(e) and 5(e). By this stage, the return flow vortex, which causes this collapse, has reached the front of the intrusion in the Corner case, while in the Slat case, it is about 4 m behind and below the surface. The delay is likely due to the greater depth of the intrusion in the Slat case, leading to a longer path for the warmed return flow. The depth of the intrusion varies along the shear layer between the intrusion and the warmed return flow. Early on there are fewer variations on the shear layer, but at later times ($t > 1800$ s) variations along the shear layer become more apparent, especially in Fig. 4(f) for the Corner case and Fig. 5(f) for the Slat case.

At the final stage, Figs. 4(g) and 4(h) and 5(g) and 5(h), the KH billows in both cases have significantly disrupted the front edge of the intrusion. In the Corner case, at $t = 2400$ s, the front position and the vortex are no longer visible in $\langle T \rangle_\theta$ [Fig. 4(g)]. In the Slat case with development slightly behind the Corner case, at $t = 2400$ s, the vortex has nearly erased the front position in $\langle T \rangle_y$ [Fig. 5(g)]. However, there are clear differences beyond the time lag between the two cases. The return flow vortex in the corner case is restricted to the depth of the intrusion, whereas, in the Slat case, the return flow vortex appears to extend below the intrusion, suggesting the possibility for enhanced vertical motion in the Slat case that goes beyond the differences in intrusion depth.

There is a clear difference between the Slat and Corner case in terms of the development of the return flow vortex. The difference in timing and proximity to the surface is controlled by the geometry of the shadowed region. This is discussed further in Sec. III C. The collapse of the intrusion in the temperature field is apparent in both cases but less severe in the Slat case. The later time behavior of the intrusions is discussed in more detail in Sec. III D.

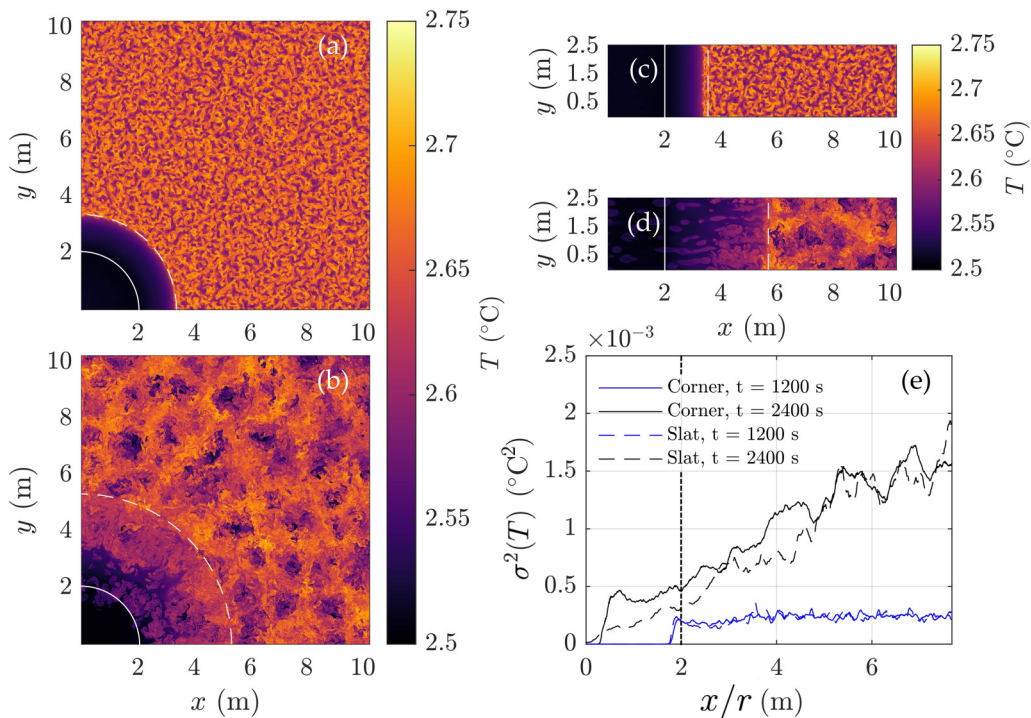


FIG. 6. Slices in the temperature field for the (a), (b) Corner and (c), (d) Slat cases. (a), (c) $t = 1200$ s and (b), (d) $t = 2400$ s. Dotted lines in the slices give the front position at the time of the slice. The solid line gives the shadow boundary, set by w_d . (e) Variance in T along the direction of propagation. The horizontal axis represents r in the Corner case and x in the Slat case. Times and cases listed in the legend. Vertical dashed line gives the shadow boundary, set by w_d .

2. Horizontal T slices

The averages given in Figs. 4 and 5 demonstrate the general behavior and evolution of the intrusion. However, they fail to capture the manner in which the intrusion develops in the transverse direction. Figure 6 gives slices in the T field, respectively, for both the Corner and Slat cases, as well as the variance in T at the same times, along the outward direction. The depths of the slices are shown in Figs. 4 and 5 using the dot-dashed line. These depths were chosen to correspond to the approximate mid depth of the intrusion at $t = 1200$ s, which is different between the two cases, hence, the slightly different depths sampled for Fig. 6.

Both the Corner and Slat cases develop similarly in the initial stages of the motion [Figs. 6(a) and 6(c)]. A relatively smooth intrusion front with features smaller than the size of convective instabilities ahead of the intrusion is evident. The intrusion front is indicated by a sharp transition between convective instabilities ahead of the intrusion and a smooth interior region. The convective instabilities are the small patches of warm and cool fluid, and are randomly shaped, rough features, oriented mostly in the vertical direction due to gravitation forces. Features along the intrusion front edge are visible and are comparable in length scale to the features ahead of the intrusion.

The temperatures in the interior of the intrusion are significantly smaller than those in the region ahead of the intrusion. The temperatures are smallest under the shadow, for radii less than 2 m in the Corner case and for x less than 2 m in the Slat case. Between the edge of the shadow boundary and the intrusion front, there exists a small gradient in temperature increasing in the direction of propagation, in both the Corner and Slat cases. As the intrusion propagates away from the shadowed boundary, the interior is gradually heated at rate of Q_0/λ . The fluid closest to the intrusion front has

been heated longer and as a result is warmer than fluid farther behind the intrusion front. A sharp change in temperature of approximately $0.1\text{ }^\circ\text{C}$ persists at the intrusion front. Based on the rate of heating of Q_0/λ , an increase in temperature of $0.1\text{ }^\circ\text{C}$ is obtained at approximately 600 s. Figure 4(a) and Fig. 5(a) both show that at $t = 600$ s, the intrusion front is only barely away from the shadow boundary.

$\sigma^2(T)$ [Fig. 6(e)] along the direction of propagation at $t = 1200$ s is similar for both cases, with a peak just before 2 m with nearly constant variance after to the end of the domain. Note that the location of the peak does not coincide with the front position. It instead corresponds to the head of the return flow. Further evidence of the intensity of this variance (which includes information from both the transverse and vertical direction) in the azimuthal and y direction is that above and below the return flow at $t = 1200$ s there are no (large) perturbations to the background temperature field. This can be seen clearly in $\langle T \rangle_\theta$ and $\langle T \rangle_y$ in Figs. 4(c) and 5(c). It is difficult to point to the intrusion front position in the variance of T at $t = 1200$ s; however, there is a slight dip in the variance of T between the intrusion front ($x/r \approx 3.4$ m) and the leading edge of the warm return flow ($x/r \approx 2$ m). The dip indicates that in the body of the return flow, there is less transverse variance in temperature compared to both the head of the return flow and the instabilities ahead of the intrusion.

At the next time ($t = 2400$ s) shown in Figs. 6(d) and 6(b), there have been significant changes in the T slices. The instabilities have grown into large convective cells with length scales $O(0.1\text{--}1\text{ m})$, typical of Rayleigh-Bénard convection which has been previously discussed in the context of RDC [52], lending visual credence to the analysis of the transition from the solar radiation-dominated phase to the convection dominated phase as an increase past a critical Rayleigh number. The length scales of these cells do not continue to grow appreciably after the CL—away from the shadow—reaches the bottom of the domain. The maximum cell size is likely set by λ/L_z but a more in-depth analysis is required to fully understand these cells and is not the focus of this paper. Features along the intrusion front have grown, and the return flow has entered the intrusion interior. There are also some differences that are identifiable between the Corner and Slat cases. The transition between the interior and exterior of the intrusion is less abrupt in the T slices for both the Corner and Slat cases. This is caused by the vortex generated by the interface between the return flow and the intrusion, visible near the front of the intrusion in $\langle T \rangle_y$ and $\langle T \rangle_\theta$ [see Figs. 4(e) and 4(g) and 5(e) and 5(g)].

The Corner and Slat cases are essentially identical, save for the geometric differences of the leading edge, at $t = 1200$ s [Figs. 6(a) and 6(c)]. At $t = 2400$ s [Figs. 6(b) and 6(d)], the RDC ahead of the intrusion is also similar. However, there is a striking difference behind and at the intrusion front at the depths chosen. In the Corner case, T is more uniform between the intrusion front at the shadow boundary, whereas in the Slat case, there are warm, round features with sharper edges. These features are new Rayleigh-Taylor instabilities forming due to the continued heating away from the shadowed region and the lower penetration of the return flow vortex leaving a region of mostly undisturbed fluid. Further, the temperature immediately behind the intrusion front is not uniform. This is due to nonuniform penetration of the return flow vortex in the vertical direction in the Slat case at the depth chosen. The sharpness at the intrusion front also is retained in the Slat case but is lost in the Corner case. This is due to the difference in depths of the return flow vortex, as well as the destruction of the intrusion front in the Corner case, or the lack thereof in the Slat case. These slices are examined in more detail in Chapter 5 of Ref. [53].

$\sigma^2(T)$ has changed significantly from earlier times at $t = 2400$ s in Fig. 6(e). At this stage, the variance gradually increases with increasing distance from the shadowed region, even past the intrusion front. This effect is not visually apparent in the T slices or in any of the averaged quantities discussed above shown in the section. We expect that the variance would be larger ahead of the intrusion front than behind it. We also expect that that variance behind the intrusion should also increase with time as it interacts with the return flow. However, the gradual increase in the variance of T past the intrusion front suggests that the presence of the intrusion is affecting the convective cells nearest to the intrusion front [Fig. 6(e)]. We expected that $\sigma^2(T)$

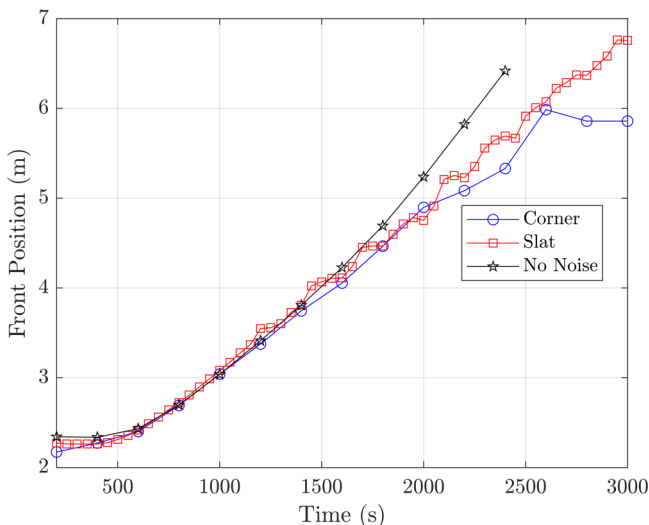


FIG. 7. Front position for all three cases listed in Table I. The method of determining the front position is explained in detail in Sec. II E. Time resolution of curves is based on output frequency from each simulation, noting that the Slat case is 4 times smaller than the No Noise and Corner cases in terms of storage.

would quickly approach a constant value as it did at earlier times. The increasing variance with distance from the shadow implies that the convective cells closer to the intrusion front are affected by the intrusion, even if it is not visually apparent, compared to those farther away. This is a surprising result that is not obvious from looking at the fields themselves; hence, it is revisited in Sec. III D.

B. Front position

The front edge of the intrusion is clearly visible at early times in both the Corner and Slat cases. The location of the front edge is uniform in the No Noise case. The location of the front edge as a function of time is compared in Fig. 7. The method for estimating the front position is outlined in Sec. II E. All three cases exhibit an initial growth phase in the first 600 s, where the rate of change of the front position with time increases (i.e., the front accelerates). The duration of the initial growth phase is identical to the one observed in Ref. [22]. This shows that the initial growth is well captured in two dimensions. In the Slat and Corner cases, the next phase is characterized by an approximately linear slope. In the No Noise case, the slope of the front position in Fig. 7 continues to increase with time. The No Noise case front position begins to diverge from Corner and Slat cases between near $t = 1500$ and 1800 s, suggesting an approximate time when convection has notably affected the propagation of the intrusion. Note that the divergence in front position occurs during the convection dominated phase but well after the transition. As shown in Fig. 2, there is no RDC in the No Noise case.

In the previous section, it was shown that there are very clear similarities and differences between the Corner and Slat case. One such difference is the development rate and height of the KH billows generated at the top edge of return flow (comparing Figs. 4 and 5). The resulting vortex catches up with the intrusion front and effectively erases it from the T field in the Corner case. The vortex in the Slat case develops similarly but at a lower height and more slowly. The manner in which it interferes with the intrusion front is also lessened, discussed in the previous section. Despite these differences, the location of the front edge of the intrusion is equal for both cases as a function of time, as shown in Fig. 7. That is, however, until about $t \approx 2500$ s, where the leading edge of the intrusion stops progressing in the Corner case. The last time shown in Fig. 4(h) is the last time in

which the front position increases in the Corner case. This is perhaps not surprising because the mechanism for generating the intrusion is a temperature gradient across the shadow boundary. At later times the temperature gradient is smeared by the effects of the vortex crashing into the intrusion front. In Sec. III D, how the intrusion stops propagating in the Corner case but continues in the Slat case is discussed in more detail.

1. Estimating a Froude number

As shown in Sec. II E 1, there does not exist a specific estimate of the Froude number for cases with time- and depth-varying density. Nonetheless, the Froude number is considered an important parameter in the analysis of gravity currents. We suggest an alternative approach to estimating a Froude number following the classical example where the available potential energy is converted entirely into kinetic energy for the current. Writing the temperature field using Eq. (11) and using the linear equation of state, Eq. (12), we equate the kinetic energy to the available potential energy

$$\frac{1}{2} w_d L_y L_z \rho_0 u_b^2 = g \int_V [\rho(z, t) - \rho_{far}(z, t)] z dV, \quad (14)$$

where $\rho_{far}(z, t)$ is an approximation to the background potential energy, obtained by assuming that the domain is sufficiently wide such that the background potential energy is determined only by the unshadowed region. Equation (14) is written for the Slat case only but can be easily converted for use in the Corner case without a change to the result.

Substituting in the parameters in Table II and solving for u_b , we recover a Buoyancy velocity which is $O(10^{-3} \text{ ms}^{-1})$ in the first 600 s, after which the intrusion interior and the region ahead of the intrusion are heated at the same rate and the density difference is approximately constant. This is the same order of magnitude as the current speed in both the Corner and Slat cases (Fig. 7 has a slope of approximately $2 \times 10^{-3} \text{ ms}^{-1}$ in both cases), resulting in a Froude number which is $O(0.1-1)$. A more in-depth study of gravity currents with time- and depth-varying density in both the intruding and ambient is necessary to determine if this is the appropriate estimation of the Froude number.

C. Intrusion depth analysis

Figures 4 and 5 establish that there is a clear difference in intrusion depth between these two cases. As discussed in Sec. II E, we define the depth of the intrusion as the average depth of the shear layer (Fig. 3) along the length of the intrusion starting at the shadow boundary and ending at the intrusion front position. Figure 8 gives the intrusion depth for all three cases considered in this paper. The first 1000 s are not shown as the intrusion depth by this definition does not produce useful results prior to this time.

The depth of gravity currents typically decreases with time [23,31]. Figure 8 clearly shows that the intrusion depth decreases only for the No Noise case. The turbulent mixing in the ambient and return flow in both the Corner and Slat cases increases the depth of the intrusion. An increase in gravity current depth due to a turbulent ambient has previously been observed and measured [23,54].

The No Noise case here acts as a point of comparison. The intrusion depth remains constant until shortly after $t = 1500$ s, where it begins to decrease. This time is close to the transition time between the solar radiation-dominated phase and the convection-dominated phase, but there is no such transition in the No Noise case. However, around this time the return flow vortex approaches the intrusion front in the No Noise case (not shown), which is shortly after at $t = 1800$ s.

The initial offset between the depth of the Slat case and the depths of the Corner and No Noise cases is explained by the geometric differences of the shadowed region. This can be shown by considering a pair of constant volume gravity currents—one with a cylindrical lock and the other with a flat lock, analogous to the Corner and Slat cases, respectively—and assuming that both propagate in equal area rectangles, similar to the assumptions made in Ref. [28]. If $L(t)$ is the

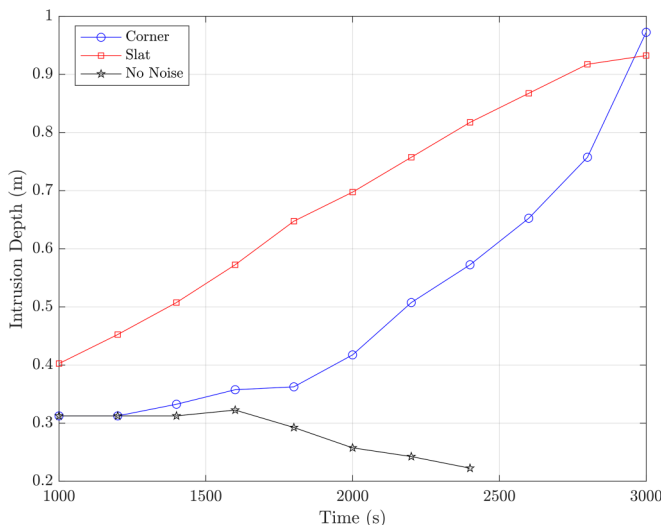


FIG. 8. Intrusion depth defined as the transition between outward and inward motion in the u_r field (Corner and No Noise case) or u (Slat case).

front position and $D(t)$ is the depth, then

$$D \propto \frac{w_d}{L}$$

in the Slat case and

$$D \propto \left(\frac{w_d}{L}\right)^2$$

in the Corner and No Noise cases. The shape of the depth in the No Noise case after $t = 1500$ s is reasonably consistent with a L^{-2} relationship and suggests that the depth of the No Noise case approximately behaves like a constant volume gravity current. A more complete discussion of the constant volume gravity current is found in the Ph.D. thesis of the first author [53].

The depth ratio between the Corner and Slat cases is w_d/L , if L is assumed to be unchanged between each case. Figure 7 shows that this is a reasonable assumption. At $t = 1000$ s, the depth ratio is $\approx 3/4$ in Fig. 8 and is acceptably close to $w_d/L = 2/3$ at the same time, using $L = 3$ m at $t = 1000$ s for both cases. After $t = 1000$ s, the depth of both the Corner and Slat cases begins to increase. In the Corner case, there is a brief flattening of the intrusion depth between $t = 1600$ and 1800 s, possibly due to the interaction between the return the vortex and the intrusion front. Evidently, the effect of the turbulent return flow is to increase the intrusion depth overtime, with a second increase in the rate of change shortly after the point in time where the outward flow of the intrusion ceases.

The slope of the intrusion depth versus time in the Slat case is nearly constant, with a small change near $t = 1800$ s. As shown by Figs. 5 and 6(b) and 6(d), the return flow vortex leaves a gap of mostly undisturbed fluid near the surface in the interior of the intrusion. If the return flow vortex is indeed responsible for the change and slope in the Corner case, it is unsurprising that we observe less of a change in the intrusion depth in the Slat case, which is able to propagate farther than the Corner case.

D. Late-time intrusion behavior

In the early stages of the simulations firmly in the solar radiation-dominated phase the driving mechanism that generates the intrusion is the density differences at the shadow boundary. These

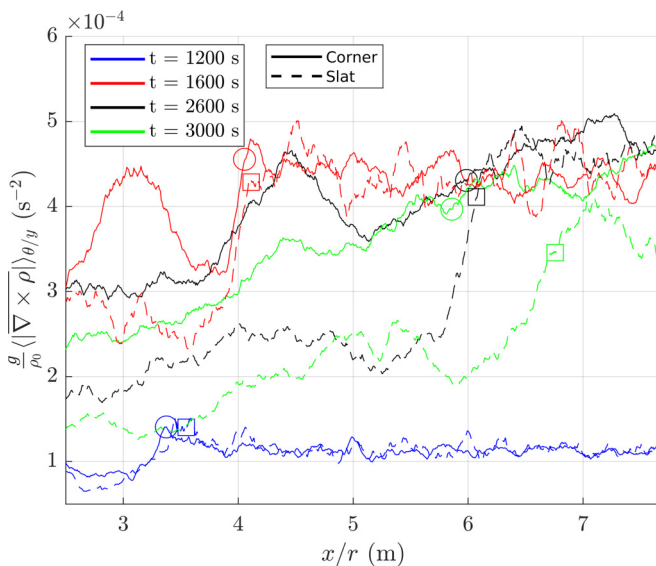


FIG. 9. Baroclinic vorticity generation, averaged in the θ (Corner case, solid lines) or y (Slat case, dashed lines) direction and the top half of the z dimension. Times are indicated by a color. The front position is indicated by a square (Slat case) or circle (Corner case) along each curve.

density differences over a small region create a sharp increase in the baroclinic vorticity term in the vorticity equation. Figure 9 shows quite clearly that after the point in time that the intrusion in the Corner case stops spreading ($t > 2400$ s) there is no longer a sharp change in the baroclinic term at the intrusion front. Meanwhile, in the Slat case the sharp increase at the intrusion front is still present, and as a result the intrusion is able to continually propagate outward. It is not the convection ahead of the intrusion that arrests the motion and continued outward flow, but instead it is the destruction of the intrusion in the temperature field by the return flow vortex that flattens the horizontal density gradients at the intrusion front along the direction of propagation.

Figure 9 shows that as a result of the return flow vortex, the density gradients in the interior of the intrusion increase, approaching the gradients in the RDC ahead of the intrusion. Even at earlier times, prior to the convection dominated phase, the magnitude of the baroclinic vorticity generation ahead of the intrusion front is comparable to the magnitude at the intrusion front, again implicating the sharp increase at the intrusion front as the source of the continued motion.

It is the efficiency of the intrusion at introducing turbulent and warm fluid into the interior of the intrusion that arrests the continued outward flow of the intrusion. Geometric differences alone between the two cases explain how the Slat case continues to propagate outwards well after the Corner case stops propagating. It should be noted that the existence of an unmixed layer [Figs. 10(f), 10(h), and 10(j)] mostly unperturbed by the turbulent return flow vortex in the Slat case is likely parameter dependent, even if we expect that the Slat case will always result in a deeper intrusion due to conservation of volume (Sec. III C). If the initial vertical and horizontal length scales of the fluid underneath the shadowed region (namely, λ and w_d) were chosen to produce a smaller volume under the shadow, it is likely that a return flow would have the capacity to destroy the intrusion in the same way as in the Corner case and arrest the continued propagation of the intrusion front. In such a scenario, the equivalent Corner case would mix with the return flow vortex and cease propagating more rapidly as well.

The evolution of the enstrophy, averaged in the transverse direction, is given in Fig. 10. The enstrophy, especially on small scales, is highly linked to dissipative effects. At each time in Fig. 10 (row by row), the stark difference is in the interior of the intrusion. In the corner case, non-negligible

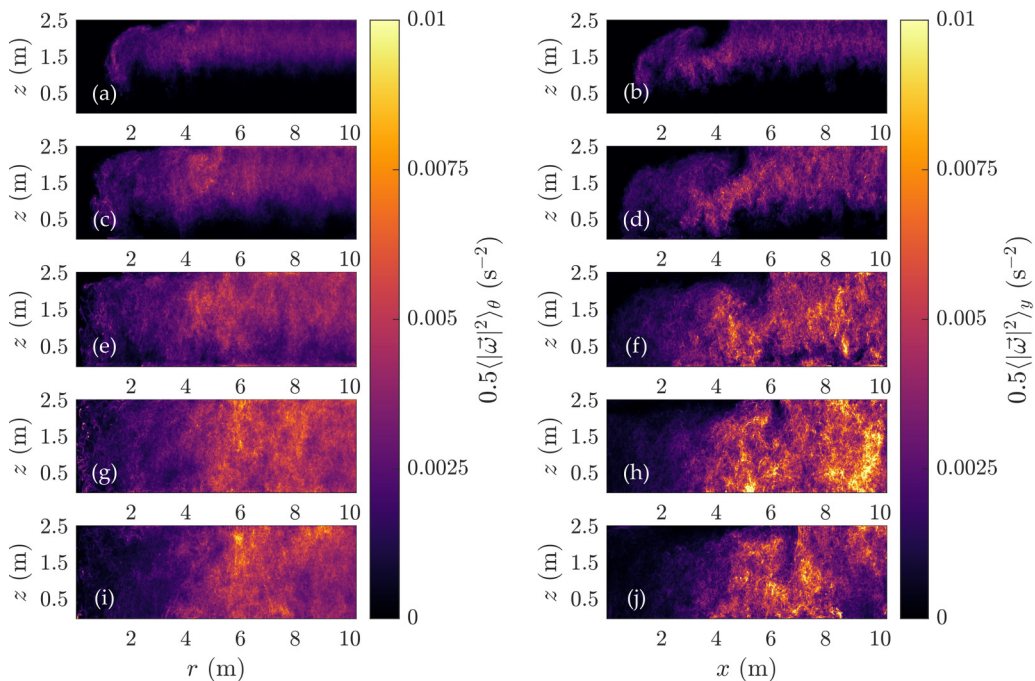


FIG. 10. Enstrophy averaged in the azimuthal or y direction for the Corner and Slat cases. (a), (b) $t = 1800$ s, (c), (d) $t = 2200$ s, (e), (f) $t = 2600$ s, (g), (h) $t = 3000$ s, and (i), (j) $t = 3400$ s. The first column (a), (c), (e), (g), (i) corresponds to the Corner case and the second column (b), (d), (f), (h), (j) corresponds to the Slat case.

values of the enstrophy are distributed throughout the domain. Unsurprisingly, the magnitude of the enstrophy behind the intrusion front is generally smaller than ahead of the intrusion front, with a positive gradient in the outward direction, reaching a maximum near $r = 6$ m at the intrusion front edge. The maximum value of the enstrophy is visible as a large mass behind the intrusion front (remnants of the return flow vortex) at $t = 1800$, 2200 , and 2600 s in Figs. 9(a), 9(c), and 9(e). After the intrusion front ceases to continue propagating outwards, the enstrophy increases at the intrusion front [Figs. 10(h) and 10(j)]. The interaction between the intrusion that is no longer flowing outwards, and the convective cells ahead of the intrusion generate a region of high enstrophy and enhanced mixing.

In the Slat case, a large pocket of low or negligible enstrophy is maintained near the intrusion front for all times shown but modified by the return flow at later times. As we previously discussed in Sec. III A, the return flow is not able to destroy the intrusion front in the temperature field in the Slat case as early as in the Corner case. As the return flow vortex continues to increase in size with time, the pocket of low enstrophy is pulled downwards along the intrusion front at $t = 3000$ and 3400 s in Figs. 9(h) and 9(j). As the intrusion front continues to propagate, no enstrophy enhancement is visible near the leading edge.

In both cases there is a significant amount of rotation on large scales behind the intrusion front. As we have just discussed, in the corner case this results in a pile up in enstrophy at the intrusion front [Figs. 10(e), 10(g), and 10(i)]. In the Slat case, the intrusion continues to propagate outwards, and the return flow vortex grows in both horizontal and vertical directions, gradually absorbing the irrotational fluid in the body of the intrusion. Vertical domain scale rotation is easily identified in $\langle w \rangle_\theta$ [Corner; Figs. 11(a) and 11(c)] and $\langle w \rangle_y$ [Slat; Figs. 11(e) and 11(g)], at $t = 2800$ s in Figs. 11(a) and 11(b) and $t = 3400$ s in Figs. 11(e) and 11(g), respectively. The rotation appears in the mean w field as a column of downward motion near the intrusion front, immediately adjacent

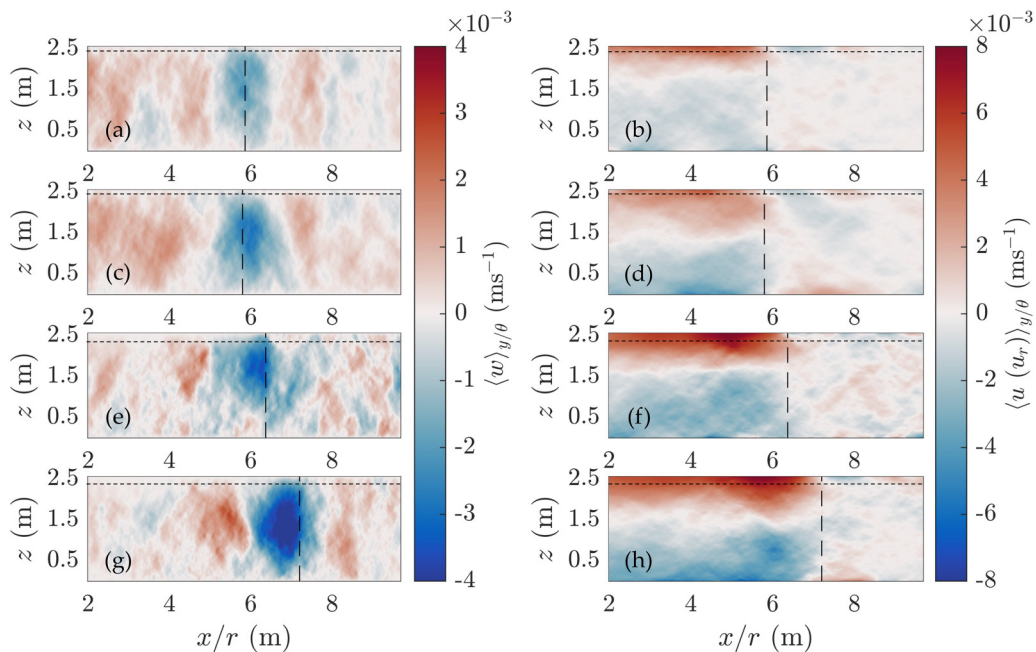


FIG. 11. w (left column) and u or u_r (right column) averaged in the azimuthal or y direction for the Corner and Slat cases. (a), (b) $t = 2800$ s for the Corner case. (c), (d) $t = 3400$ s for the Corner case, (e), (f) $t = 2800$ s for the Slat case, and (g), (h) $t = 3400$ s for the Slat case. Vertical dashed line indicates the front position of the intrusion, and the horizontal dashed line corresponds to the depth of slices in Fig. 12.

and a rapid transition to a neighboring column of upward motion, farther behind the intrusion front [towards the left in Figs. 11(a), 11(c), 11(e), and 11(g)].

There are two important features in this rotation that should be noted. First, this is an average, and as shown by Figs. 12(c) and 12(d) there is significant variations in w in the interior of the intrusion, close to the intrusion front. Second, in the corner case the column of downward flow is centered on the intrusion front, but in the Slat case this column is centered just behind the intrusion front. The relative position of the intrusion front and the convective downwelling cell indicates clear interactions between the intrusion and the convective cells ahead of the intrusion front. The layer of outward flow along the surface in $\langle u \rangle_\theta$ [Figs. 11(b) and 11(d)] is directly connected to the return flow by the downwelling cell, through the convective region ahead of the intrusion front. Conversely, in the Slat case the intrusion and return flow interact behind the intrusion front.

There are many ways in which this interaction is apparent in the data. One way is the development of a vertical column of upward motion (again on average) in $\langle w \rangle_\theta$, clearly ahead of the intrusion front, in Figs. 11(a) and 11(c). A similar effect is also clear at the later time of $t = 3400$ s in the Slat case in Fig. 11(g). Connected columns of upwards or downwards flow is not seen farther ahead of the intrusion front in either case.

The fields shown in Fig. 11 are averages in the transverse direction. At the depths indicated by the horizontal dashed lines in Fig. 11, slices of the w and u_r fields (u for the Slat case) are given in Fig. 12. These slices paint a particular picture of the motion immediately ahead of the intrusion front, especially in the corner case [Figs. 12(a) and 12(c)]. Ahead of the intrusion, large convective cells develop. Upward motion is a collection of large clumps bounded by these regions of downward motion, in a honeycomb pattern. As these convective cells approach the surface, the solid boundary forces the upward flow to move outwards.

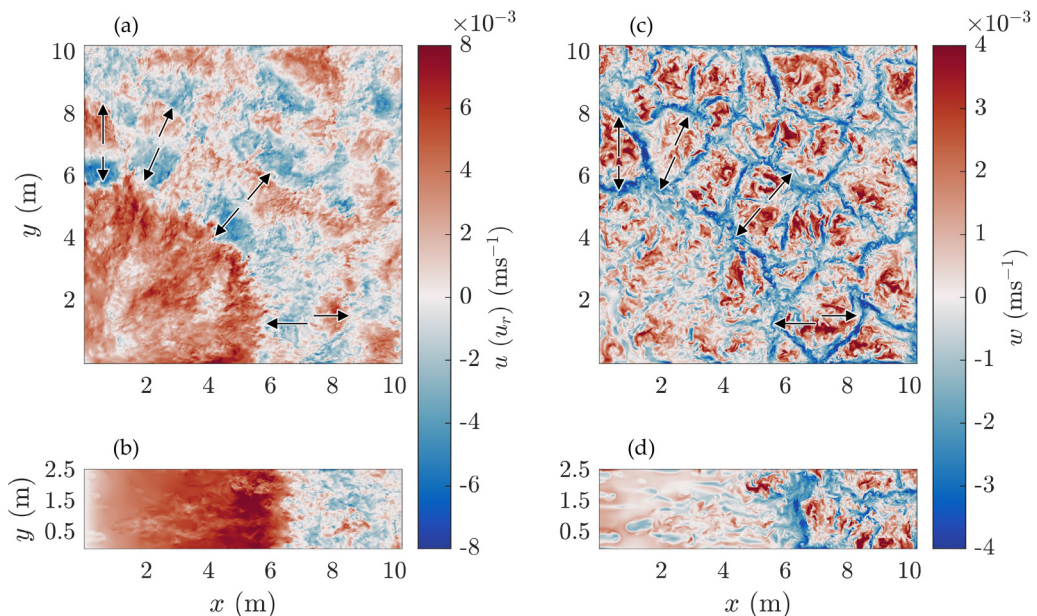


FIG. 12. u or u_r (a), (b) and w (c), (d) slices for the Corner (a), (c) and Slat (b), (d) cases at $t = 3000$ s. Slices are taken at the depth shown by the horizontal dashed line in Figs. 4 and 5.

The u_r slice [Fig. 12(a)] shows that these clumps are bisected in the azimuthal direction at the approximate midpoint in the radial direction. Arrows are drawn on the u_r slice and copied to the same location in the w slice [Fig. 12(b)] to show the correlation of flow towards the intrusion front. These convective cells are behaving like a fountain of water reaching its peak. Note that this inward flow due to the upwelling convective cells is not equally strong along the arc of the intrusion front. Inward flow ahead of the intrusion front is notably weaker for angles (as measured from the x axis) less than 45° .

Convective cells without arrows have notably weaker (or nonexistent) inward flow than those that do. This emphasizes the variability along the intrusion front due to convection ahead of the intrusion. Convection ahead of the intrusion front in the Slat case is of similar strength in both the upward and downward direction [Fig. 12(d)]. However, flow in the negative x direction due to these upward convective cells is nonexistent [Fig. 12(b)]. As it was just noted, this does happen in the corner case but only in small areas. Hence, the lack of significant inward flow in the Slat case could be a result of random variations and as a result a wider domain is necessary to fully analyze the inward flow generated up upwelling convective cells close to the surface.

IV. DISCUSSION AND CONCLUSIONS

In this paper, three simulations are presented that examine the effect of heterogeneous solar radiation intensity extended into three dimensions. One simulation has a rectangular shadow (Slat case), another has a quarter circle shadow (Corner case), and the last one also has a quarter circle shadow, but the initial conditions do not have noise added (No Noise case) as a controlled point of comparison. Figures 2 and 3 show the motion in the initial stages ($t = 600$ to 1400 s), mostly confined to the solar radiation dominated phase. In this phase, an intrusion flows away from the shadowed region in all three cases, as in two dimensions, with a parabolic leading edge. A return flow develops in the reverse direction and can be divided into two parts. A warm return flow immediately beneath the intrusion and a cool return flow towards the bottom. In all three cases, the head of the warm return flow forms into a shape similar to a Rayleigh-Taylor instability, bisected

by the thin shear layer between the intrusion and warm return flow. Radiatively driven convection ahead of the intrusion is not sufficiently strong to significantly affect the propagation of the intrusion. Figure 2 shows that the velocity scale in the interior of the intrusion greatly exceeded the velocity scales in the return flow and in the radiatively driven convection ahead of the intrusion. The front position at this stage for all three cases is identical (Fig. 7).

There are two important structural differences prior to $t = 1400$ s. The first is between the No Noise and noisy cases (Corner and Slat) where there are features ahead of the intrusion and in the body of the warm return flow in the noisy cases and none in the No Noise case (by construction). The average taken in the transverse direction for each noisy case reveals the Rayleigh-Taylor-like shape at the head of the warm return flow [Figs. 4(c) and 5(c)]. The variations in the warm return flow in the transverse direction increase the height of the body of the warm return flow [Figs. 2(g)–2(i), 4(c), and 5(c)]. The intrusion front, despite the features in the convection ahead of the intrusion, is comparatively smooth prior to $t = 1400$ s, likely due to the difference in velocity scales between the intrusion and the convection ahead of the intrusion.

The second difference is in the intrusion height, defined as the depth of the shear interface between the intrusion and the warm return flow. Prior to $t = 1400$ s, the Slat case is noticeably deeper than both the Corner and No Noise cases. This difference can be entirely attributed to volume conservation. Assuming a fixed volume intrusion, in the Corner case the depth is inversely proportional to the square of the intrusion length, whereas in the Slat case, it is inversely proportional to the length.

As the intrusion continues to propagate, convection ahead of the intrusion begins to affect how the intrusion develops. The intrusion front position of the No Noise case begins to diverge from the Corner and Slat cases (Fig. 7 past $t = 1500$ s and the depth of the shear layer gradually increases (Fig. 8). Radiatively driven convection ahead of the intrusion front decreases temperatures compared to pure solar radiation. This reduction in temperature ahead of the intrusion front reduces the magnitude of the baroclinic term in the direction of propagation, and hence, stops the intrusion front speed from continuing to increase. The depth of the shear layer gradually increases as a result of the convection at the intrusion front, contrary to classical gravity current set-ups where the gravity current depth gradually decreases [23,31]. It has been shown that turbulence ahead of a gravity current causes its depth to increase [23] and a similar effect is observed here and shown clearly by comparing u_r and u at later times (right column of Fig. 11) to u_r and u earlier (right column of Fig. 4 or 5).

The comparison between the Corner and Slat cases highlighted that the differences in geometry lead to differences in intrusion height. The main consequence of this difference is the manner in which the return flow vortex interacts with the intrusion and the surface. In both cases, the return flow vortex is generated along the shear layer and eventually catches up to the intrusion front position. In the Corner case, the return flow vortex reaches the surface and erases the intrusion from the temperature field [Figs. 4(g) and 6(b)], although a positive gradient in the radial direction remains. However, in the Slat case, the return flow vortex does not reach the surface, nor does it completely eliminate the intrusion from the temperature field [Figs. 5(g) and 6(d)]. Instead, the intrusion in the Slat case continues to propagate (Fig. 7), allowing a thin and low enstrophy region to propagate farther into the ambient [Figs. 10(f), 10(h), and 10(j)]. It is then possible to speculate that the effect of increasing the intrusion depth, regardless of geometry, results in an intrusion that is able to propagate farther. As shown by Fig. 7, as a result of the return flow vortex reaching the surface, the intrusion almost suddenly stops propagating. This suggests that there exists a critical lifetime of an intrusion of this type, rather than a gradual slowdown that one might expect of a classical gravity current [23,31,55].

The broader research community has not, to date, considered horizontal variations in optical properties in the interior of ice-covered lakes and their effect on the distribution of heat and the generation of currents, other than Ref. [22]. Previous work has considered variations near the shore or in shallow regions [14,32,56]. From the work presented in this paper, one can see that variations in optical properties in the interior of a quiescent lake leads to the generation of robust horizontal currents, or intrusions. These intrusions distribute cool fluid away from the shadowed region, and

warm fluid under the shadow. This could potentially lead to faster melt rates in areas with shorter optical thicknesses (less radiation) and slower melt rates in areas with longer optical thicknesses (more radiation), which is contrary to what is expected. Further, these intrusions also provide a mechanism for distributing nutrients and other suspended materials laterally. The capacity for the distribution of heat under the shadowed region depends on geometry. The shallower Corner case injects heat and turbulent fluid much closer to the surface compared with the Slat case and, hence, would have a larger impact on melt rates. Radiatively driven convection is mostly a vertical process (see the convective cells formed ahead of the intrusion front as well as [20,22,52,57,58]) prior to interacting with solid boundaries, with limited horizontal scale. By considering variations in optical properties—caused by ice thickness, clarity, and snow cover—we have presented a mechanism for horizontal transport in small, ice-covered lakes.

Further research should consider a more realistic top boundary. The model SPINS we used for the simulations presented in this paper is capable of imposing both no-slip velocity and $T = 0^\circ\text{C}$ conditions at the surface, a common approach to modeling ice in direct numerical simulations [18,32,58]. It would also be possible to introduce some degree of roughness to the surface. Including melt water or changing ice-depth is not currently possible in SPINS but should also be considered for a full description of dynamics at the ice-water interface. The effect of such an upper boundary introduces a boundary layer and would lead to the growth of the lobe and cleft instability [23,33], modifying the shape of the intrusion front near the boundary and possibly how it interacts with the convective cells.

This paper also contributes to the gravity current literature, albeit less directly. The analysis of gravity currents with time-varying density differences did not exist in the literature (to the authors' knowledge) prior to Ref. [22]. Horizontal variations in solar radiation intensity with a quiescent background state—typically of ice-covered lakes in the morning and immediately after snow melts at the surface—represent a geophysically relevant example of a gravity current with time-varying density differences driving motion. Another example could occur in ice-covered water bodies with high salinity, like the oceans. Melting ice freshens the water beneath it, and vice versa for freezing. If this occurs at the edge of a glacier or ice floe, density differences could drive a surface gravity current similar to the one studied in this paper.

ACKNOWLEDGMENTS

This work was supported by NSERC Discovery Grant RGPIN-311844-37157 and computational resources obtained via a resource allocation competition, funded by the Digital Research Alliance of Canada. The authors would also like to thank the two anonymous reviewers whose suggestions have led to substantial improvements to this paper.

-
- [1] J. J. Magnuson, D. M. Robertson, B. J. Benson, R. H. Wynne, D. M. Livingstone, T. Arai, R. A. Assel, R. G. Barry, V. Card, E. Kuusisto, N. G. Granin, T. D. Prowse, K. M. Stewart, and V. S. Vuglinski, Historical trends in lake and river ice cover in the Northern Hemisphere, *Science* **289**, 1743 (2000).
 - [2] D. R. Mueller, P. Van Hove, D. Antoniadis, M. O. Jeffries, and W. F. Vincent, High Arctic lakes as sentinel ecosystems: Cascading regime shifts in climate, ice cover, and mixing, *Limnol. Oceanogr.* **54**, 2371 (2009).
 - [3] M. Leppäranta, *Freezing of Lakes and the Evolution of Their Ice Cover* (Springer, Berlin/Heidelberg, Germany, 2015).
 - [4] R. I. Woolway and C. J. Merchant, Worldwide alteration of lake mixing regimes in response to climate change, *Nat. Geosci.* **12**, 271 (2019).
 - [5] R. I. Woolway, B. M. Kraemer, J. D. Lenters, C. J. Merchant, C. M. O'Reilly, and S. Sharma, Global lake responses to climate change, *Nat. Rev. Earth Environ.* **1**, 388 (2020).
 - [6] C. R. Duguay, T. D. Prowse, B. R. Bonsal, R. D. Brown, M. P. Lacroix, and P. Ménard, Recent trends in Canadian lake ice cover, *Hydrol. Processes* **20**, 781 (2006).

- [7] M. J. Hewer and W. A. Gough, Lake Ontario ice coverage: Past, present and future, *J. Great Lakes Res.* **45**, 1080 (2019).
- [8] Y. Dibike, T. Prowse, T. Saloranta, and R. Ahmed, Response of Northern Hemisphere lake-ice cover and lake-water thermal structure patterns to a changing climate, *Hydrol. Processes* **25**, 2942 (2011).
- [9] C. R. Duguay, G. M. Flato, M. O. Jeffries, P. Ménard, K. Morris, and W. R. Rouse, Ice-cover variability on shallow lakes at high latitudes: Model simulations and observations, *Hydrol. Processes* **17**, 3465 (2003).
- [10] M. Leppäranta, A. Terzhevik, and K. Shirasawa, Solar radiation and ice melting in Lake Vendyurskoe, Russian Karelia, *Hydrol. Res.* **41**, 50 (2010).
- [11] S. Karetnikov, M. Leppäranta, and A. Montonen, A time series of over 100 years of ice seasons on Lake Ladoga, *J. Great Lakes Res.* **43**, 979 (2017).
- [12] I. Caramatti, F. Peeters, D. Hamilton, and H. Hofmann, Modelling inter-annual and spatial variability of ice cover in a temperate lake with complex morphology, *Hydrol. Processes* **34**, 691 (2020).
- [13] G. Kirillin, M. Leppäranta, A. Terzhevik, N. Granin, J. Bernhardt, C. Engelhardt, T. Efreмова, S. Golosov, N. Palshin, P. Sherstyankin, G. Zdorovenнова, and R. Zdorovenнов, Physics of seasonally ice-covered lakes: A review, *Aquat. Sci.* **74**, 659 (2012).
- [14] G. B. Kirillin, A. L. Forrest, K. E. Graves, A. Fischer, C. Engelhardt, and B. E. Laval, Axisymmetric circulation driven by marginal heating in ice-covered lakes, *Geophys. Res. Lett.* **42**, 2893 (2015).
- [15] D. Bouffard and A. Wüest, Convection in lakes, *Annu. Rev. Fluid Mech.* **51**, 189 (2019).
- [16] D. Bouffard, G. Zdorovenнова, S. Bogdanov, T. Efreмова, S. Lavanchy, N. Palshin, A. Terzhevik, L. R. Vinnå, S. Volkov, A. Wüest, R. Zdorovenнов, and H. N. Ulloa, Under-ice convection dynamics in a boreal lake, *Inland Waters* **9**, 142 (2019).
- [17] D. Bouffard, R. E. Zdorovenнов, G. E. Zdorovenнова, N. Pasche, A. Wüest, and A. Y. Terzhevik, Ice-covered Lake Onega: Effects of radiation on convection and internal waves, *Hydrobiologia* **780**, 21 (2016).
- [18] H. N. Ulloa, K. B. Winters, A. Wüest, and D. Bouffard, Differential heating drives downslope flows that accelerate mixed-layer warming in ice-covered waters, *Geophys. Res. Lett.* **46**, 13872 (2019).
- [19] K. B. Winters, H. N. Ulloa, A. Wüest, and D. Bouffard, Energetics of radiatively heated ice-covered lakes, *Geophys. Res. Lett.* **46**, 8913 (2019).
- [20] D. M. Farmer, Penetrative convection in the absence of mean shear, *Q. J. R. Meteorolog. Soc.* **101**, 869 (1975).
- [21] A. P. Grace, M. Stastna, K. G. Lamb, and K. A. Scott, Numerical simulations of the three-dimensionalization of a shear flow in radiatively forced cold water below the density maximum, *Phys. Rev. Fluids* **7**, 023501 (2022).
- [22] D. J. M. Allum, A. P. Grace, and M. Stastna, Two-dimensional simulations of flow in ice-covered lakes with horizontal variations in surface albedo, *Phys. Rev. Fluids* **7**, 103501 (2022).
- [23] J. E. Simpson, *Gravity Currents: In the Environment and the Laboratory* (Cambridge University Press, 1999).
- [24] J. E. Simpson, Effects of the lower boundary on the head of a gravity current, *J. Fluid Mech.* **53**, 759 (1972).
- [25] L. F. R. Espath, L. C. Pinto, S. Laizet, and J. H. Silvestrini, Two- and three-dimensional direct numerical simulation of particle-laden gravity currents, *Comput. Geosci.* **63**, 9 (2014).
- [26] A. Dai and C.-S. Wu, High-resolution simulations of cylindrical gravity currents in a rotating system, *J. Fluid Mech.* **806**, 71 (2016).
- [27] R. Inghilesi, C. Adduce, V. Lombardi, F. Roman, and V. Armenio, Axisymmetric three-dimensional gravity currents generated by lock exchange, *J. Fluid Mech.* **851**, 507 (2018).
- [28] H. E. Huppert and J. E. Simpson, The slumping of gravity currents, *J. Fluid Mech.* **99**, 785 (1980).
- [29] H. E. Huppert, The propagation of two-dimensional and axisymmetric viscous gravity currents over a rigid horizontal surface, *J. Fluid Mech.* **121**, 43 (1982).
- [30] H. E. Huppert, Gravity currents: A personal perspective, *J. Fluid Mech.* **554**, 299 (2006).
- [31] M. I. Cantero, J. R. Lee, S. Balachandar, and M. H. Garcia, On the front velocity of gravity currents, *J. Fluid Mech.* **586**, 1 (2007).
- [32] C. L. Ramón, H. N. Ulloa, T. Doda, K. B. Winters, and D. Bouffard, Bathymetry and latitude modify lake warming under ice, *Hydrol. Earth Syst. Sci.* **25**, 1813 (2021).

- [33] N. Castro-Folker, A. P. Grace, and M. Stastna, Three-dimensional structure of cold-water gravity currents, *Phys. Rev. Fluids* **8**, 113901 (2023).
- [34] A. P. Grace, M. Stastna, K. G. Lamb, and K. A. Scott, Asymmetries in gravity currents attributed to the nonlinear equation of state, *J. Fluid Mech.* **915**, A18 (2021).
- [35] A. P. Grace, M. Stastna, K. G. Lamb, and K. A. Scott, Gravity currents in the cabbelling regime, *Phys. Rev. Fluids* **8**, 014502 (2023).
- [36] C. J. Subich, K. G. Lamb, and M. Stastna, Simulation of the Navier–Stokes equations in three dimensions with a spectral collocation method, *Int. J. Numer. Methods Fluids* **73**, 103 (2013).
- [37] C. Xu, M. Stastna, and D. Deepwell, Spontaneous instability in internal solitary-like waves, *Phys. Rev. Fluids* **4**, 014805 (2019).
- [38] D. Brydon, S. Sun, and R. Bleck, A new approximation of the equation of state for seawater, suitable for numerical ocean models, *J. Geophys. Res.: Oceans* **104**, 1537 (1999).
- [39] S. MacIntyre, J. O. Sickman, S. A. Goldthwait, and G. W. Kling, Physical pathways of nutrient supply in a small, ultraoligotrophic arctic lake during summer stratification, *Limnol. Oceanogr.* **51**, 1107 (2006).
- [40] A. Cortés and S. MacIntyre, Mixing processes in small arctic lakes during spring, *Limnol. Oceanogr.* **65**, 260 (2020).
- [41] T. Von Karman, The engineer grapples with nonlinear problems, *Bull. Am. Math. Soc.* **46**, 615 (1940).
- [42] T. Maxworthy, J. S. J. E. Leilich, J. E. Simpson, and E. H. Meiburg, The propagation of a gravity current into a linearly stratified fluid, *J. Fluid Mech.* **453**, 371 (2002).
- [43] V. K. Birman, E. Meiburg, and M. Ungarish, On gravity currents in stratified ambients, *Phys. Fluids* **19**, 086602 (2007).
- [44] P. T. Zubkov and E. V. Kalabin, Numerical investigation of the natural convection of water in the neighborhood of the density inversion point for Grashof numbers up to 106, *Fluid Dyn.* **36**, 944 (2001).
- [45] Y.-P. Hu, Y.-R. Li, and C.-M. Wu, Rayleigh–bénard convection of cold water near its density maximum in a cubical cavity, *Phys. Fluids* **27**, 034102 (2015).
- [46] Y.-R. Li, Y.-P. Hu, Y.-Q. Ouyang, and C.-M. Wu, Flow state multiplicity in Rayleigh–Bénard convection of cold water with density maximum in a cylinder of aspect ratio 2, *Int. J. Heat Mass Transf.* **86**, 244 (2015).
- [47] L. N. Trefethen, *Spectral Methods in MATLAB* (Society for Industrial and Applied Mathematics, Philadelphia, 2000).
- [48] J. P. Boyd, *Chebyshev and Fourier Spectral Methods* (Dover Publications Inc, Mineola, NY, 2000).
- [49] M. I. Cantero, S. Balachandar, and M. H. Garcia, High-resolution simulations of cylindrical density currents, *J. Fluid Mech.* **590**, 437 (2007).
- [50] P. K. Kundu and I. M. Cohen, *Fluid Mechanics* (Academic Press, San Diego, California, 2002).
- [51] C. Härtel, E. Meiburg, and F. Necker, Analysis and direct numerical simulation of the flow at a gravity-current head. Part 1. Flow topology and front speed for slip and no-slip boundaries, *J. Fluid Mech.* **418**, 189 (2000).
- [52] V. Bouillaut, S. Lepot, S. Aumaître, and B. Gallet, Transition to the ultimate regime in a radiatively driven convection experiment, *J. Fluid Mech.* **861**, R5 (2019).
- [53] D. Allum, Simulations of radiatively driven convection and spatially heterogeneous solar radiation intensity in ice-covered lakes, Ph.D. thesis, University of Waterloo, 2023.
- [54] P. F. Linden and J. E. Simpson, Gravity-driven flows in a turbulent fluid, *J. Fluid Mech.* **172**, 481 (1986).
- [55] B. M. Marino, L. P. Thomas, and P. F. Linden, The front condition for gravity currents, *J. Fluid Mech.* **536**, 49 (2005).
- [56] H. N. Ulloa, G. Constantinescu, K. Chang, D. Horna-Munoz, O. Hames, and A. Wüest, Horizontal transport under wind-induced resonance in stratified waterbodies, *Phys. Rev. Fluids* **5**, 054503 (2020).
- [57] D. Mironov, A. Terzhevik, G. Kirillin, T. Jonas, J. Malm, and D. Farmer, Radiatively driven convection in ice-covered lakes: Observations, scaling, and a mixed layer model, *J. Geophys. Res.: Oceans* **107**, 7 (2002).
- [58] A. A. Smirnovsky, S. I. Smirnov, S. R. Bogdanov, N. I. Pal’shin, R. E. Zdorovenov, and G. E. Zdorovenova, Numerical simulation of turbulent mixing in a shallow lake for periods of under-ice convection, *Water Resour.* **50**, 768 (2023).